ACS APPLIED ENERGY MATERIALS

www.acsaem.org Article

Efficient Liquid-Junction Monolithic Cobalt-Mediated Dye-Sensitized Solar Cells for Solar and Artificial Light Conversion

Fátima Santos, Carolina Hora, Dzmitry Ivanou,* and Adélio M. Mendes*

Cite This: *ACS Appl. Energy Mater.* 2021, 4, 5050−5058 Read Online

ACCESS | Metrics & More | Article Recommendations | Supporting Information

ABSTRACT: Due to the extremely high power conversion efficiency under indoor light, aesthetic appeal, and safety, the mature technology of dye-sensitized solar cells (DSSCs) is now considered as one of the most budding technologies to address the fast-growing need for cordless power in countless IoT devices and wireless sensors. The monolithic design of DSSCs (M-DSSCs) is technologically attractive for commercial production offering straightforward processing in-series modules, low cost, and compactness. The advancements in liquid-junction M-DSSCs reported so far are related only to conventional Ru-dye and I_3^-/I^- electrolyte devices. The present study reports a M-DSSC incorporating a Co(III)/(II)$(bpy)_3$ redox shuttle and a YD2-*o*-C8 porphyrin dye and developed using commercial materials. The apparent activation energy for electron transfer, electron charge-transfer resistance, and exchange current density on FTO−Pt nanoparticles, Pt metal, graphite/carbon-black, and PEDOT:PSS in the cobalt electrolyte were determined to identify the favorable counter-electrode. The impact of the electrical spacer layers made from conventional ZrO_2 and highly reflective rutile TiO_2 on the photocurrent quantum yield was also assessed. The recombination-suppressing additive concentration in the electrolyte and photoanode sensitization conditions were thoroughly optimized to render M-DSSC devices with a photocurrent conversion efficiency of 9.5% under 1-sun illumination, which is by far the highest reported for M-DSSCs. The high power conversion efficiency of ca. 22% was attained under 1000 lx artificial light, making the developed M-DSSCs very attractive for indoor use.

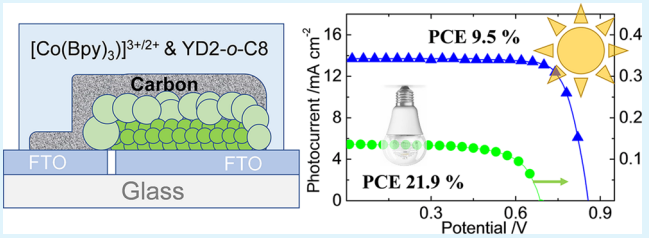

KEYWORDS: *dye-sensitized solar cells, monolithic, cobalt redox electrolyte, activation energy, counter-electrode, porphyrin sensitizer*

1. INTRODUCTION

Dye-sensitized solar cells (DSSCs) are third-generation photovoltaic devices featuring low cost, ease of fabrication, and environmental friendliness.[1,2] Due to the decent power conversion efficiency (PCE) of scattered and dim light, which is much superior to the PCE of silicon,[3,4] DSSCs are considered a feasible approach for outdoor building-integrated photovoltaics.[5,6] Recently, the exponentially growing number of low-power-consumption electronic devices, such as the Internet of Things (IoT) and wireless sensors to name a few, turned the development of cordless powering strategies for indoor applications absolutely relevant. It triggered the development of DSSCs as favorable indoor photovoltaic devices.[7] DSSCs effectively compete with other PV technologies offering an amazingly high PCE of ca. 30% under artificial light;[2,8−10] they have a pleasant colorful appearance and the ability to be incorporated into semitransparent and flexible devices,[11] could be aesthetically integrated into the working and living interior, and are safe, in the sense that they are free from toxic soluble lead or tin compounds.

Since the seminal breakthrough in 1991,[12] decades of research on DSSCs has led to the certified PCE of ca. 12%,[13] still employing the family of Ru-dyes and iodine electrolyte discovered at the outset.[12,14] The renaissance of DSSCs happened with the discovery of new one-electron transfer high-potential redox shuttles and dyes with high extinction coefficients, broad absorption spectra, and electron recombination suppressing behavior.[15,16] The state-of-the-art best-performing DSSCs are liquid-junction devices with Co(III)/Co(II) and Cu(II)/Cu(I) redox shuttles for generating a high output potential of ca. 1 V.[10,17] Cobalt redox couples and porphyrin sensitizers allow attaining a PCE of 13%;[16,17] implementation of cosensitization strategies with thienoindols yielded a PCE as high as 14.2%.[18] DSSCs with a Cu(II)/Cu(I) redox mediator were presented in 2005,[19] and, at present, they are achieving a promising PCE of ca. 13%.[8−10]

Efficient DSSCs are assembled in a so-called "conventional" architecture where the photoanode and the counter-electrode, each on a separate conducting glass, are placed opposite to each other with a microgap in between and the electrolyte filling this gap. In an alternative design, the so-called "monolithic" (M-

Received: March 2, 2021
Accepted: May 3, 2021
Published: May 13, 2021

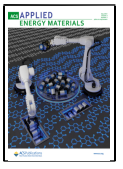

https://doi.org/10.1021/acsaem.1c00616
ACS Appl. Energy Mater. 2021, 4, 5050−5058

DSSCs) design, the photoanode and the counter-electrode are on the same glass and an electrical spacer layer is used to separate both electrodes.[11] The monolithic arrangement allows a ca. 30% reduction in material cost[20] and is very straightforward for assembly in a modular configuration,[11] making it the most promising architecture for upscaling these devices. However, the PCE of M-DSSCs is below that of their conventional counterparts,[21−24] primarily due to the spacer layer. The spacer layer creates an extra resistance for electrolyte diffusion, increasing the charge transport resistance, and inefficiently scatters unabsorbed light back to the photoanode.

Since the first reported M-DSSCs in 1996[25] with a PCE of 6.7%, they have progressed due to the development of new catalytic and low-cost counter-electrodes[21−23] and electrical spacer layers.[24,26,27] Implementation of counter-electrodes made from platinized graphite/carbon-black resulted in a PCE of 7.6%;[21] physically attached PEDOT films and platinized Cr foil counter-electrodes allowed reaching a PCE of 7.7 and 8.0%, respectively.[22,23] The use of a highly reflective electrical spacer layer rendered a M-DSSC with the highest reported PCE of 8.3%.[27] Surprisingly, all of the advances in liquid-junction M-DSSCs are presented so far only for the original archetype of iodine-mediated devices.

In this work, we report M-DSSCs built using a Co(III/II)tris(bipyridyl) redox shuttle and porphyrin sensitizer YD2-*o*-C8. Cobalt-mediated monolithic devices require reference devices with high PCEs, which preferably should be feasible for assembly from readily existing commercial parts and reactants. The challenge of producing efficient M-DSSCs from solely commercially available materials is addressed. The most commonly used materials in DSSC electrocatalysts were assessed for counter-electrodes—Pt nanoparticles, Pt metal foil, graphite/carbon-black, and PEDOT:PSS; the exchange current density and apparent activation energy were determined and correlated with the performance of M-DSSCs. To the best of our knowledge, we are reporting for the first time on the apparent activation energy of Pt, graphite/carbon-black, and PEDOT:PSS catalysts for electron transfer in $[Co(bpy)_3]^{(3+/2+)}$ complexes. Spectral distribution of the photocurrent quantum yield revealed an efficient electrical spacer layer made from polydisperse rutile particles. Dye loading time and electrolyte composition were optimized to produce a record-breaking liquid-junction monolithic device displaying a 1-sun PCE of 9.5%, which is the highest of monolithic-type DSSCs reported so far. A PCE of ca. 22% was attained under artificial 1000 lx light, making the developed M-DSSCs very attractive and straightforward for indoor light conversion.

2. EXPERIMENTAL SECTION

2.1. Reagents and Materials. FTO-coated glasses (TEC-7; 7 Ω·sq^{-1}) and screen-printable TiO_2 pastes (30NR-D and WER2-O) were purchased from GreatCell Solar. Titanium diisopropoxide bis(acetylacetonate), anhydrous isopropyl alcohol, acetylacetone, lithium perchlorate, dimethyl sulfoxide (≥99.90%), 4-*tert*-butylpyridine (TBP), and lithium perchlorate ($LiClO_4$, 99.90%) were purchased from Sigma-Aldrich. Screen-printable graphite/carbon-black paste (Elcocarb B/SP), platinum nanoparticle paste (Platisol T/SP), and zirconium dioxide paste (Zr-Nanoxide ZR/SP), as well as the hot-melt sealant (Meltonix 1170-60, 60 μm Surlyn) were from Solaronix. Co(II/III)tris(bipyridyl)tetracyanoborate complexes (Eversolar Co-200 and Co-300) and the donor−π-bridge−acceptor zinc porphyrin sensitizer (YD2-*o*-C8) were acquired from Everlight. Titanium tetrachloride (99.90%, Acros Organics) and PEDOT:PSS aqueous solution (Clevios) were from Fluka.

2.2. Fabrication of DSSCs. M-DSSC devices were assembled according to the configuration described elsewhere.[27] An 80 ± 5 nm TiO_2 blocking layer was deposited by spray pyrolysis at 450 °C. The precursor solution was composed of 7.0 mL of anhydrous isopropyl alcohol, 0.6 mL of titanium diisopropoxide bis(acetylacetonate), and 0.4 mL of acetylacetone. After the spray deposition, the TiO_2 layer was annealed at 450 °C for 45 min.

A mesoporous TiO_2 (30NR-D paste, 7 ± 1 μm) layer with an active area of 0.13 cm^2 was deposited by screen-printing and sintered at 500 °C for 1 h. Then, the TiO_2 films were immersed in a 40 mM $TiCl_4$ aqueous solution at 70 °C for 30 min, dried, and annealed at 500 °C for 1 h.

An opaque ZrO_2 layer (Zr-Nanoxide ZR/SP, 6 ± 1 μm) and a scattering reflector TiO_2 layer (WER2-O, 6 ± 1 μm) were used as commercial electrical spacers. The platinum counter-electrode layer was deposited by DC magnetron sputtering; the graphite/carbon-black (Elcocarb B/SP) layer was deposited by doctor-blading and sintered for 45 min at 420 °C; and the PEDOT:PSS layer was formed by spin-coating of PEDOT:PSS commercial solution (Clevios) mixed with 5% of DMSO, followed by annealing at 120 °C for 15 min.

Sensitization was performed using a fresh solution of 0.2 mM YD2-*o*-C8 dye in ethanol/toluene (volume ratio, 3:1). Then, the M-DSSCs were rinsed in absolute ethanol, dried in a N_2 flow, and sandwiched with an ordinary glass using a hot-pressed thermoplastic sealant. The electrolyte was composed of 0.165 M Co(II) and 0.045 M Co(III) tris(bipyridyl)tetracyanoborate complexes, 0.8−1.4 M TBP, and 0.1 M $LiClO_4$. After electrolyte injection through the predrilled holes in the ordinary glass, the holes were sealed with a thermoplastic film and a lamella glass.

2.3. Fabrication of Symmetrical Half-Cells. The materials used as the counter-electrodes were deposited on FTO substrates by different techniques: platinum metal by DC magnetron sputtering, the platinum nanoparticle (Platisol T/SP) layer by doctor-blading, the graphite/carbon-black (Elcocarb B/SP) layer by screen-printing, and the PEDOT:PSS layer by spin-coating. Two identical FTO substrates coated with the same material were sandwiched using a thermoplastic sealant. The electrolyte was injected through the predrilled holes in one of the electrodes, and the holes were sealed.

2.4. Characterization. The photovoltaic performance of the M-DSSC was characterized under simulated solar light (AM1.5G, 100 mW·cm^{-2}) from a Solar Simulator MiniSol (LSH-7320, Newport) and under artificial light (600 and 1000 lx) using a LED lamp (Osram, Class A+, 60 W, 2700 K) as a light source. A radiometer Delta Ohm HD 2102.2 was used to determine the power of the light derived from the LED lamp. A Zennium (Zahner) electrochemical station was used to record photocurrent vs potential characteristics.

The electrochemical impedance spectra were collected in the dark at −0.80 V using an Autolab electrochemical station (PGSTAT 302 N, Metrohm), and ZView software was used to analyze the impedance spectra. The incident photon to current conversion efficiency (IPCE) spectra were recorded using a semiautomatic station (Newport). Measurements were performed at 2 nm wavelength intervals between 300 and 800 nm.

The electrocatalytic activity of counter-electrodes was analyzed in the temperature range between −5 and 60 °C, measuring the electrochemical impedance spectra at 0 V bias using symmetrical half-cells. An in-house made experimental setup[28] was used to control the operating temperature of the half-cells.

The surface morphology of the counter-electrode materials was analyzed using a Quanta 400 FEG ESEM microscope. The reflectance spectra of the electrical spacer layers were measured using a Shimadzu UV-3600 spectrophotometer equipped with an LISR-3100 integrating sphere, with $BaSO_4$ powder compact used for the baseline.

3. RESULTS AND DISCUSSION

3.1. Characterization of Counter-Electrodes for M-DSSCs. The counter-electrode in a M-DSSC should provide efficient electrochemical regeneration of Co(III) species continuously produced at the photoanode. Seminal works on

https://doi.org/10.1021/acsaem.1c00616
ACS Appl. Energy Mater. 2021, 4, 5050−5058

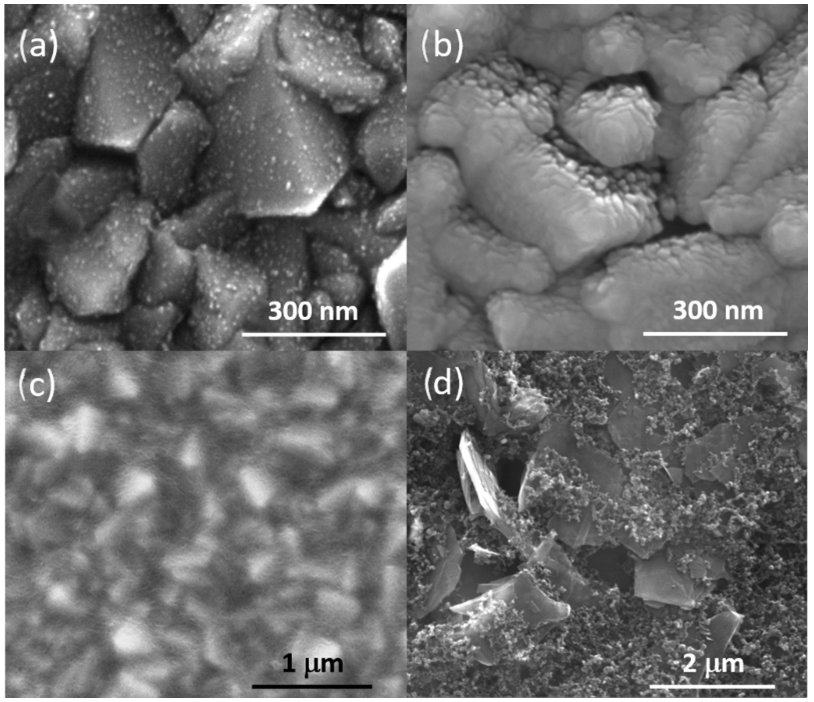

Figure 1. Top-view SEM images of Pt_{NP} (a), Pt_{Met} (b), PEDOT:PSS (c), and GCB (d) on FTO glass.

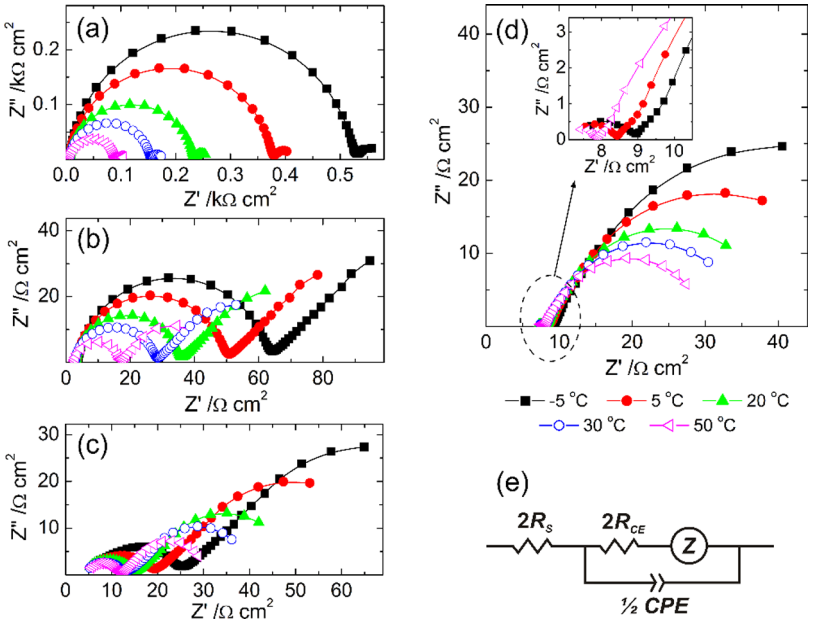

Figure 2. Typical Nyquist plots for the EIS response of dummy cells with electrodes made from Pt_{NP} (a), Pt_{Met} (b), PEDOT:PSS (c), and GCB (d) and the equivalent electrical circuit[31] used for fitting the spectra (e).

cobalt-mediated DSSCs report a surprisingly high PCE of ca. 10−12% for devices assembled with conventional counter-electrodes made from thermally activated Pt nanoparticles (Pt_{NP}) on FTO glass.[29,30] Further studies suggest that Pt_{NP} counter-electrodes show insufficient electrochemical activity to reduce Co(III) complexes.[31−39] More efficient counter-electrodes have been reported based on graphene,[31,32] tellurium−graphene composite,[33] PEDOT[34] and PEDOT−graphene composite,[35] poly(3,4-alkylthiophenes),[36] polyaniline,[37] carbon-black,[38] and carbon−graphene composite.[39] The present report assesses the use of Pt_{NP} deposited on FTO, Pt metal film (P_{Met}), graphite/carbon-black (GCB) composite, and PEDOT:PSS.

Apart from the electrocatalytic activity toward the redox reaction, the specific surface area of the counter-electrode is critical as polarization and charge-transfer resistances decrease with the interfacial area between the electrode and electrolyte.[34,35] The morphology of the electrodes was studied by SEM. Figure 1 presents the secondary electron SEM image for the selected materials.

Conventional thermal activation of the electrode with platinum leads to the formation of a very sparse layer of Pt particles with sizes of ca. 8 nm (Figure 1a). The Pt film obtained

https://doi.org/10.1021/acsaem.1c00616
ACS Appl. Energy Mater. 2021, 4, 5050−5058

by magnetron sputtering overlays the substrate, repeating the FTO topography (Figure 1b). The PEDOT:PSS coating produces a smooth continuous layer (Figure 1c). The graphite/carbon-black (GCB) coating is highly heterogeneous with the most developed surface among the materials; carbon-black nanoparticles randomly distributed over graphite microplates ensure high porosity and large specific surface area (Figure 1d). The thicknesses of the layers determined from the cross section of the samples were 0.1, 0.3, and 15 μm for Pt_{Met}, PEDOT:PSS, and GCB layers, respectively.

The electrochemical and electrocatalytic activity of the cathode materials were analyzed in thin symmetrical half-cells.[31,33,40−42] Regarding the counter-electrode, good electrochemical activity means the ability of the electrode to yield a high current density with minimal losses of the applied potential. This is typically assessed either by the exchange current density (J_0) or the charge-transfer resistance (R_{CT}), which are related by eq 1[31,42]

$$J_0 = \frac{RT}{nFR_{CT}} \quad (1)$$

where R is the universal gas constant, T is the temperature, n is the number of electrons, and F is the Faraday constant. Both R_{CT} and J_0 depend on the electrode effective surface area, indicating that the same material prepared with a higher specific surface area will show lower R_{CT} and higher current density. Apart from the developed surface, the electrochemical activity of the counter-electrode is primarily related to the catalytic properties of the material used, which means that the catalytic activity of this material increases as the apparent activation energy (E_a) of the charge transfer decreases, as shown by eq 2[42]

$$J_0 = J_{inf} \cdot \exp\left(-\frac{E_a}{RT}\right) \quad (2)$$

where J_{inf} is the J_0 at infinite temperature. The apparent activation energy, E_a, is the most important factor related to the catalytic activity as it appears in the exponential term of eq 2. Surprisingly, no estimates of E_a values for the counter-electrode materials in cobalt electrolytes have been reported so far. The Arrhenius equation (eq 2) allows the determination of E_a from the temperature dependence of J_0, where J_0 could be calculated using eq 1 from R_{CT}.

To determine the R_{CT} values, electrochemical impedance spectroscopy (EIS) of the symmetrical half-cells was performed. Figure 2 shows the impedance response at different temperatures for the half-cells with Pt_{NP}, Pt_{Met}, GCB, and PEDOT:PSS electrodes.

For all materials studied, the Nyquist diagrams display two well-defined features. The first one appears at high frequencies as a semicircle close to the origin of the plot and assigned to the R_{CT} at the electrode/electrolyte interface. The second feature appears at medium frequencies and is related to ionic diffusion. In cells with Pt_{NP}, Pt_{Met}, and PEDOT:PSS electrodes, this feature starts as a line close to ca. 45° and bends downward the abscissa axis for lower frequencies. Such a pattern is typical for space-confined diffusion; the finite-length Warburg element $\mathbf{Z}$ is equal to W_S in Figure 2e. In the cells with GCB electrodes, the Nyquist shape in the diffusion region fits better to the de Levie's model for semi-infinite length[43] and in Figure 2e, $Z = L_o$, which is completely consistent with the porous structure and thickness of a few microns of the GCB film. The EIS response of the half-cells was fitted to the equivalent circuits in Figure 2e; the R_{CT} values at different temperatures were extracted from the model, and J_0 values were calculated using eq 1 and are listed in Table S1. Figure 3 shows the Arrhenius plots for the J_0 values with different electrodes.

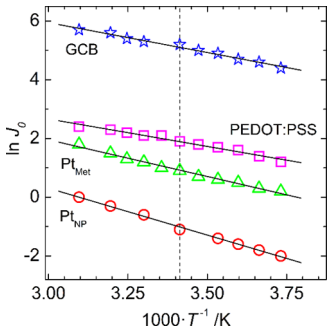

Figure 3. Arrhenius plots of the J_0 values for different counter-electrodes. The vertical dashed line drawn for a room temperature of 20 °C is to guide the eye.

The Arrhenius behavior as a function of temperature (in the range: −5 to 60 °C) is observed for all materials studied. The E_a values for electron transfer obtained for Pt_{NP}, Pt_{Met}, PEDOT:PSS, and GCB are 26.5, 20.7, 15.6, and 16.9 kJ·mol^{-1}, respectively, revealing PEDOT:PSS as the best catalyst among the studied ones for the reduction of $Co(bpy)_3^{3+}$; the GCB electrode displays only a slightly lower performance. The sputtered Pt_{Met} electrodes show a decent catalytic activity toward $Co(bpy)_3^{3+}$ reduction (E_a = 20.7 kJ·mol^{-1}). It is worth noting that Pt_{NP} electrodes formed by thermal decomposition of H_2PtCl_6 are the least active catalysts. The highest E_a of Pt_{NP} is more likely due to the conventional thermal platinization, which typically leaves ca. 20% of the platinum surface passivated as $PtCl_2$ and $PtCl_4$.[44]

3.2. Performance of M-DSSCs with Pt_{Met}, PEDOT:PSS, and GCB Counter-Electrodes. Figure 4 presents the photocurrent vs applied potential (I−V) curves for M-DSSCs assembled with counter-electrodes of Pt_{Met}, GCB, and PEDOT:PSS. As a space layer, the conventional opaque ZrO_2 (6 ± 1 μm) was used.

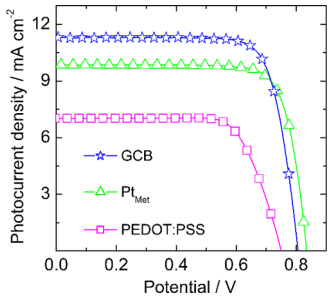

Figure 4. I−V curves of M-DSSCs with different counter-electrodes.

The metrics of the photovoltaic performance were extracted from I−V curves and are summarized in Table 1.

M-DSSCs with the sputtered Pt_{Met} electrode display a V_{OC} of 0.84 V, a J_{SC} of 9.8 mA·cm^{-2}, and a FF of 0.79, resulting in a PCE of 6.5%. The device with an electrode made from GCB displays the highest J_{SC} (J_{SC} = 11.3 mA·cm^{-2}) and a PCE of 7.1%. Surprisingly, despite the highest catalytic activity of PEDOT:PSS, M-DSSCs with this electrode showed the weakest

https://doi.org/10.1021/acsaem.1c00616
ACS Appl. Energy Mater. 2021, 4, 5050−5058

Table 1. Photovoltaic Metrics of M-DSSCs and Resistances (in Ω·cm^2) of the Devices with Different Counter-Electrodes

counter-electrode	V_{OC}/V	J_{SC}/mA·cm^{-2}	FF	PCE/%	R_S	R_{CE}	R_K	R_{EL}
Pt_{Met}	0.84	9.8	0.79	6.5	7.4	12.7	75.6	45.6
GCB	0.81	11.3	0.78	7.1	10.4	28.9	82.4	40.1
PEDOT:PSS	0.75	7.0	0.73	3.8	44.7	117.7	450.7	1288

photocurrent and a PCE of only ca. 4%. An EIS study was performed to identify the effect of the counter-electrodes on the device performance (Figure 5a).

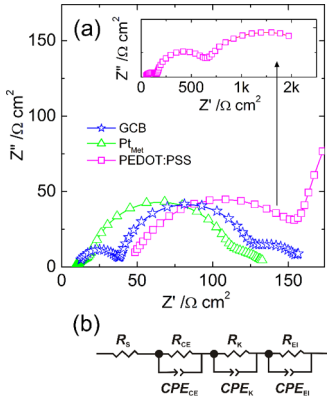

Figure 5. EIS responses in Nyquist plots of M-DSSCs with different counter-electrodes (a). Solid lines show fits to the equivalent circuit[45−47] presented in (b).

The equivalent electrical circuit presented in Figure 5b fits well the EIS spectra.[45−47] The elements in the model represent series resistance (R_S), charge-transfer resistance at the electrolyte/counter-electrode interface (R_{CE}), recombination resistance at the photoanode/electrolyte interface (R_K), and the diffusion resistance in the electrolyte (R_{El}); CPE_{CE}, CPE_K, and CPE_{El} are the respective constant phase elements. Resistances of the equivalent circuit elements obtained by fitting impedance response are summarized in Table 1.

In a M-DSSC with counter-electrodes of PEDOT:PSS, all internal resistances of the device are incredibly high, yielding a low overall performance. This was related to the way the PEDOT:PSS layer was applied. During the deposition of the PEDOT:PSS solution over the spacer layer, the polymer penetrates the layer and clogs the pores. This hinders the charge transport in both counter-electrode/electrolyte and photoanode/electrolyte interfaces, preventing the diffusion of the electrolyte; high R_{CE}, R_K, and R_{EL} resistances support this interpretation of the observed low performance. The PEDOT:PSS film prepared by spin-coating on the spacer layer had poor integrity originating from high R_S and low V_{OC}.

The devices assembled with Pt_{Met} and GCB electrodes show similar values of R_S, R_K, and R_{EL}. A low R_S value of ca. 10 Ω·cm^2 indicates that the conductivity of the 15 μm GCB layer is comparable to that of the solid 100 nm Pt layer obtained by sputtering. Practically identical for both devices, R_K is ca. 80 Ω·cm^2 and R_{EL} is ca. 40−45 Ω·cm^2, indicating that the photoanode/electrolyte interface and diffusion of the electrolyte through the spacer layer are not affected by the counter-electrode. The R_{CE} on the GCB of ca. 30 Ω·cm^2 is higher than the R_{CE} of 13 Ω·cm^2 on the Pt_{Met} electrode. This is opposite to the R_{CT} values obtained for the dummy cells, ca. 0.2 and 9 Ω·cm^2 for GCB and Pt_{Met}, respectively (Table S1). This is because, in the dummy cells, the surface of the electrode is exposed to the electrolyte, while in the M-DSSC device, the counter-electrode is monolithically attached to the porous spacer. A higher R_{CE} causes loss of potential, specifically at low current densities; as a result, the V_{OC} of the device with the GCB electrode is slightly lower than the V_{OC} of the M-DSSCs with Pt_{Met} (Figure 4). Nevertheless, the developed surface of the GCB counter-electrode ensures a high rate for the diffusion-limited process; a higher saturation photocurrent is achieved (Figure 4), rendering a device with a PCE of 7.1%. Further improvements were achieved by optimizing the electrical spacer layer, the photoanode sensitization time, and the concentration of the recombination-suppressing additive.

3.3. Spacer Layer in M-DSSCs. The PCE of M-DSSCs is significantly affected by the electrical spacer layer.[23,24,27] The spacer layer must be insulating to prevent the electron flow between the photoanode and the counter-electrode, porous to ensure a good flow of ions between electrodes, and light-reflective to direct unabsorbed light back to the photoelectrode for more efficient light harvesting.

Figure 6a presents the $I-V$ response of the devices with commercial ZrO_2 and TiO_2 spacer layers and the GCB counter-electrode. A spacer made from porous titania improved the J_{SC}

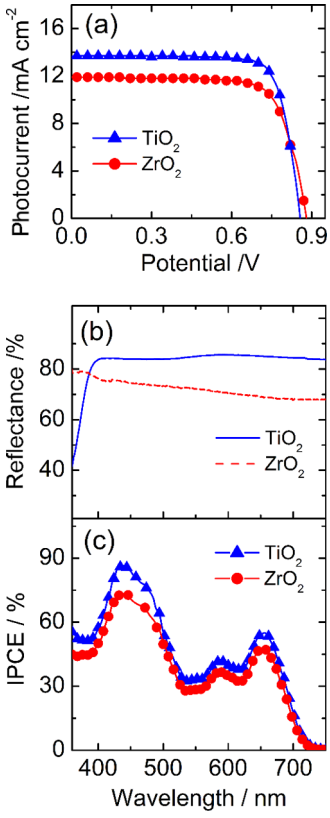

Figure 6. $I-V$ curves (a), the reflectance of the TiO_2 and ZrO_2 electrical spacer layers (b), and the IPCE spectra of M-DSSCs with different spacer layers (c).

https://doi.org/10.1021/acsaem.1c00616
ACS Appl. Energy Mater. 2021, 4, 5050−5058

up to ca. 13.9 mA·cm^{-2}, while the M-DSSCs with the ZrO_2 layer display a J_{SC} of 11.9 mA·cm^{-2}.

Considering that titania and zirconia spacers have an identical thickness of ca. 6 μm and practically the same morphology and porosity (Figure S1), the improvement of the photocurrent with the TiO_2 spacer was attributed to its higher reflectivity when compared with ZrO_2 (Figure 6b). The titania spacer contains scattering particles of rutile, which has one of the highest refractive indexes of ca. 2.8,[48,49] contributing to better light scattering and reflection. The reflectivity of the titania spacer is superior to that of zirconia at wavelengths above 400 nm; therefore, more unabsorbed light is reflected to the photoanode leading to the uniform increase of the IPCE response in the spectral range 400−750 nm (Figure 6c), which renders M-DSSCs to routinely display a PCE of 9.0% and a champion device with a PCE of 9.5%.

In the last couple of years, DSSCs have been established as one of the most promising PV devices for indoor applications.[7−10] Being a recent trend, none of the standard indoor-light sources were yet recognized. We recorded the $I-V$ curves of M-DSSC devices with indoor light using a LED lamp with an intensity of 600 lx (175 μW·cm^{-2}) and 1000 lx (286 μW·cm^{-2}) (Figure 7). The PCE was determined considering the ratio of the maximum power delivered by the device to the incident light power of the LED lamp.

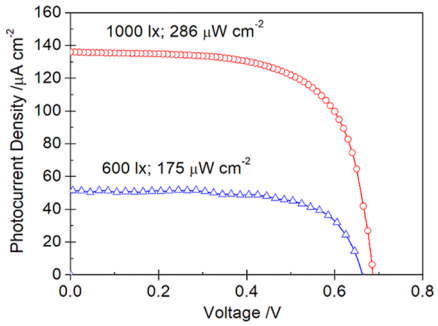

Figure 7. $I-V$ curves of the M-DSSC device under artificial light with different light intensities.

M-DSSCs with an average of 1-sun PCE of 9.0%—champion cells displayed 9.5% of PCE—displayed the maximum output powers of 22.8 and 62.7 μW·cm^{-2} and PCEs of 13.0 and 21.9% under 600 and 1000 lx, respectively. It is worth noting that the artificial light PCEs derived from M-DSSCs have achieved and even slightly surpassed the PCEs of the recently reported counterparts, assembled in a priori more efficient conventional configurations,[50,51] with the use of, however, an expensive Pt metal film as a counter-electrode.

3.4. Sensitization of Photoanodes in M-DSSCs. The sensitization conditions must ensure good dye loading at the photoanode for effective light absorption and efficient photocurrent generation.[52,53] Excessive dye adsorption leads to the agglomeration of the dye molecules, which causes quenching of the excited states and decreases electron injection into TiO_2. Dye agglomerates clog the mesopores in the photoanode, preventing electrolyte diffusion, dye regeneration, and charge transfer at the photoanode. It is possible to effectively mitigate the excessive dye adsorption controlling the sensitization time.[52] For the conventionally assembled device, the optimum time for TiO_2 sensitization using YD2-*o*-C8 dye solution was determined to be 12−16 h,[29] when the mesoporous TiO_2 layer was directly exposed to the sensitizing solution. In M-DSSCs, dye delivery to the TiO_2 occurs through the porous spacer and counter-electrode layers. Then, the sensitization time has to be optimized for the monolithic architecture,[27] a crucial parameter often neglected by researchers. Figure 8 shows the normalized metrics (PCE, J_{SC}, V_{OC}, and FF) of M-DSSCs vs time of sensitization in YD2-*o*-C8 solution.

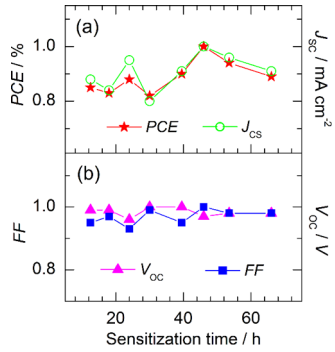

Figure 8. Normalized PCE and J_{SC} (a), V_{OC} and FF (b) of M-DSSCs vs sensitization time.

After 16 h of sensitization, M-DSSCs display rather low photocurrent and the FF values indicate insufficient dye loading. The tested M-DSSCs show the highest PCE after ca. 46 ± 2 h of sensitization, which is mainly related to the current density (Figure 8a); however, a small drop in V_{OC} and FF is also observed (Figure 8b). After 48 h of sensitization, J_{SC} starts to drop (Figure 8a), which should be related to the dye aggregation onset.

3.5. Concentration of the Recombination-Suppressing Additive in the Electrolyte. The cobalt electrolyte 4-*tert*-butylpyridine (TBP) is used to suppress the back electron recombination, increase the concentration of electrons on the conduction band of TiO_2, and attain high V_{OC} and decent photocurrents.[29,54−57] An increase in the TBP concentration increases the amount of TBP adsorbed on the TiO_2 surface, increasing the recombination resistance at the TiO_2/electrolyte interface, improving the V_{OC} up to ∼1 V.[54] Koh et al.[55] reported that excessive TBP concentration decreases the diffusion of Co species and reduces the photocurrent. The optimum concentration of TBP in conventional DSSCs was determined to be ca. 0.8 M.[29] Our study suggests that this could not be straightforwardly translated to M-DSSCs, and adjusting the TBP concentration is crucial for achieving high PCE.

Table 2 presents the normalized photovoltaic parameters of M-DSSCs loaded with electrolytes containing different concentrations of TBP (from 0.8 to 1.4 M).

The highest PCE was observed at a TBP concentration of 1.2 M. EIS of M-DSSCs was performed to identify the effect of TBP concentration on the M-DSSC performance (Figure 9).

The Nyquist plots show typical patterns with three capacitive semicircles, which are associated with the interfacial charge transfer and diffusion in the electrolyte, as described in Section 3.2 (Figure 5). The assigned values to the corresponding resistances are summarized in Table 2. The series resistance of the devices (R_S) is not affected by TBP. The interfacial resistances R_{CE}, R_K, and resistance R_{EL} gradually increase with the TBP concentration. Higher interfacial resistances are due to the TBP adsorption on the photoanode[56] and the counter-electrode,[57,58] and higher transport resistance in the electrolyte

https://doi.org/10.1021/acsaem.1c00616
ACS Appl. Energy Mater. 2021, 4, 5050−5058

Table 2. Normalized Photovoltaic Metrics of M-DSSCs at Different TBP Concentrations in the Electrolyte; the Resistances (in Ω·cm^2) Were Obtained by Fitting the Model (Figure 5b) to the Nyquist Plots (Figure 9) of the Corresponding Devices

[TBP]/M	V_{OC}/V	J_{SC}/mA·cm^{-2}	FF	PCE/%	R_S	R_{CE}	R_K	R_{El}
0.8	0.96	0.90	1.00	0.88	6.2	53.9	46.2	25.6
1.0	0.92	0.86	0.99	0.81	6.5	59.5	53.7	23.5
1.2	1.00	1.00	0.97	1.00	6.9	111.2	77.0	48.5
1.4	1.00	0.88	0.99	0.90	6.7	123.0	115.5	40.6

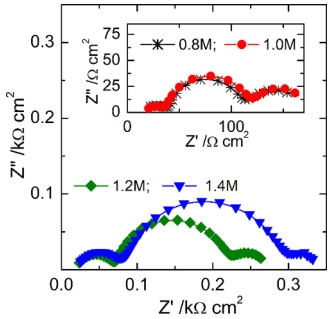

Figure 9. Nyquist diagrams for the EIS response of M-DSSCs with different TBP concentrations in the electrolyte.

(R_{EL}) originates from the increased viscosity of the electrolyte.[55] It is worth noting that with an increase of TBP concentration from 0.8 to 1.0 M, the resistances R_{CE}, R_K, and R_{EL} increase slightly but at a TBP concentration of 1.2 M there is a considerable increase, rendering the cells with the highest photovoltaic parameters. In comparison with conventional counterparts, monolithic cells require a higher optimum concentration of TBP, which might be because of the TiO_2 spacer layer with a developed surface and thick porous GCB counter-electrode. TiO_2 effectively adsorbs TBP,[56] significantly reducing the available concentration for the electrolyte, and the carbon counter-electrode may contribute as well in the TBP adsorption from the electrolyte.[58]

3.6. Stability of Cobalt-Mediated M-DSSCs. The history of PCEs in the devices was followed during 1000 h under natural aging (Figure 10). Within the first 24 h, the PCE slightly increases, which is a typical behavior of DSSCs.[59]

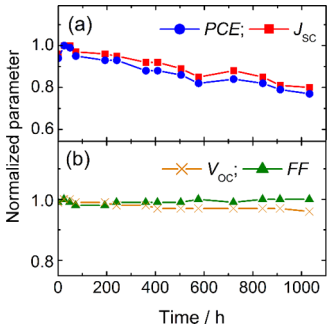

Figure 10. History of PCEs and J_{SC} (a), and V_{OC} and FF (b) for cobalt-mediated M-DSSCs.

During aging, the PCE was mostly affected by the decrease in the photocurrent (Figure 10a), which is most likely due to the acetonitrile leakage through polymeric sealants.[60] The V_{OC} remained practically constant, while the FF suffered a slight decrease of up to 600 h of aging (Figure 10b). The PCE deterioration factor determined from the declination of the plot is relatively high, ca. 1.6×10^{-4} per day. The stability of the devices should be addressed in future studies by preventing electrolyte leakage using the highly hermetic laser-assisted encapsulation with glass materials recently developed by the authors;[61,62] alternatively, quasi-solid state electrolytes may be implemented.[50,51]

4. CONCLUSIONS

The challenge of preparing highly efficient liquid-junction cobalt-mediated monolithic DSSCs, using commercially available materials, was addressed. The electrochemical activity of conventional counter-electrodes, light-reflecting properties of the electrical spacer layers, photoanode sensitization conditions, and the concentration of back electron recombination suppressing additive in the electrolyte were studied and optimized. Conventional counter-electrodes made from Pt nanoparticles, Pt metal film, graphite/carbon-black composite, and PEDOT:PSS display apparent activation energies of 26.5, 20.7, 16.9, and 15.6 kJ·mol^{-1}, respectively, in the reduction of $Co(bpy)_3^{3+}$. Extremely low saturation current densities were obtained while using the Pt nanoparticle electrode, making it an inappropriate choice for preparing an efficient device. The use of Pt and graphite/carbon-black counter-electrode layers allowed reaching decent photocurrents and PCEs of ca. 6.5 and 7%, respectively. An unexpectedly low PCE of ca. 4% was obtained with the PEDOT:PSS electrode due to its infiltration on the spacer layer, which clogs the pores hindering the charge transport and electrolyte diffusion. The highly reflecting electrical spacer layer made from rutile TiO_2, counter-electrode of graphite/carbon-black, and optimized photoanode sensitization conditions and recombination-suppressing additive (4-*tert*-butylpyridine) concentration rendered a M-DSSC with a record-breaking PCE of 9.5% under 1-sun illumination and a decent PCE of 21.9% under 1000 lx artificial light.

■ ASSOCIATED CONTENT

Supporting Information

The Supporting Information is available free of charge at https://pubs.acs.org/doi/10.1021/acsaem.1c00616.

Values of charge-transfer resistance (R_{CE}) and exchange current density (J_0) at different temperatures; SEM images of the electrical spacer layers (PDF)

■ AUTHOR INFORMATION

Corresponding Authors

Dzmitry Ivanou − *LEPABE, Departamento de Engenharia Química, Faculdade de Engenharia, Universidade do Porto Rua Dr. Roberto Frias, 4200-465 Porto, Portugal;* orcid.org/0000-0002-5313-4016; Phone: +351 920427795; Email: ivanou@fe.up.pt; Fax: +351 225081449

Adélio M. Mendes − *LEPABE, Departamento de Engenharia Química, Faculdade de Engenharia, Universidade do Porto Rua Dr. Roberto Frias, 4200-465 Porto, Portugal;*

https://doi.org/10.1021/acsaem.1c00616
ACS Appl. Energy Mater. 2021, 4, 5050−5058

orcid.org/0000-0003-2472-3265; Email: mendes@fe.up.pt

Authors

Fátima Santos − *LEPABE, Departamento de Engenharia Química, Faculdade de Engenharia, Universidade do Porto Rua Dr. Roberto Frias, 4200-465 Porto, Portugal;* orcid.org/0000-0002-9029-4107

Carolina Hora − *LEPABE, Departamento de Engenharia Química, Faculdade de Engenharia, Universidade do Porto Rua Dr. Roberto Frias, 4200-465 Porto, Portugal;* orcid.org/0000-0002-2124-7593

Complete contact information is available at: https://pubs.acs.org/10.1021/acsaem.1c00616

Notes

The authors declare no competing financial interest.

■ ACKNOWLEDGMENTS

The authors acknowledge the financial support from the "SunStorage" project, POCI-01-0145-FEDER-016387, funded by the European Regional Development Fund (ERDF) through COMPETE2020; the projects POCI-01-0145-FEDER-006939, NORTE-01-0145-FEDER-000005, and LEPABE-2-ECO-INNOVATION were all funded by FEDER funds through COMPETE 2020 and the Materials Centre of the University of Porto. This work was also financially supported by the UIDB/00511/2020 Energy—LEPABE—funded by national funds through the FCT/MCTES (PIDDAC); F.S. and C.H. acknowledge the FCT for their Ph.D. grants (reference SFRH/BD/132388/2017 and SFRH/BD/129761/2017, respectively).

■ REFERENCES

(1) Sharma, K.; Sharma, V.; Sharma, S. S. Dye-Sensitized Solar Cells: Fundamentals and Current Status. *Nanoscale Res. Lett.* **2018**, *13*, No. 381.

(2) Mariotti, N.; Bonomo, M.; Fagiolari, L.; Barbero, N.; Gerbaldi, C.; Bella, F.; Barolo, C. Recent Advances in Eco-Friendly and Cost-Effective Materials towards Sustainable Dye-Sensitized Solar Cells. *Green Chem.* **2020**, *22*, 7168−7218.

(3) Toyoda, T.; Sano, T.; Nakajima, J.; Doi, S.; Fukumoto, S.; Ito, A.; Tohyama, T.; Yoshida, M.; Kanagawa, T.; Motohiro, T.; Shiga, T.; Higuchi, K.; Tanaka, H.; Takeda, Y.; Fukano, T.; Katoh, N.; Takeichi, A.; Takechi, K.; Shiozawa, M. Outdoor performance of large scale DSC modules. *J. Photochem. Photobiol., A* **2004**, *164*, 203−207.

(4) Cornaro, C.; Bartocci, S.; Musella, D.; Strati, C.; Lanuti, A.; Mastroianni, S.; Penna, S.; Guidobaldi, A.; Giordano, F.; Petrolati, E.; Brown, T. M.; Reale, A.; Carlo, A. D. Comparative analysis of the outdoor performance of a dye solar cell mini-panel for building integrated photovoltaics applications. *Prog. Photovolt.: Res. Appl.* **2015**, *23*, 215−225.

(5) Kim, J.-H.; Han, S.-H. Energy Generation Performance of Window-Type Dye-Sensitized Solar Cells by Color and Transmittance. *Sustainability* **2020**, *12*, No. 8961.

(6) Acciari, G.; Adamo, G.; Ala, G.; Busacca, A.; Caruso, M.; Giglia, G.; Imburgia, A.; Livreri, P.; Miceli, R.; Parisi, A.; Pellitteri, F.; Pernice, R.; Romano, P.; Schettino, G.; Viola, F. Experimental Investigation on the Performances of Innovative PV Vertical Structures. *Photonics* **2019**, *6*, No. 86.

(7) Mathews, I.; Kantareddy, S. N.; Buonassisi, T.; Peters, I. M. Technology and Market Perspective for Indoor Photovoltaic Cells. *Joule* **2019**, *3*, 1415−1426.

(8) Freitag, M.; Teuscher, J.; Saygili, Y.; Zhang, X.; Giordano, F.; Liska, P.; Hua, J.; Zakeeruddin, S. M.; Moser, J. E.; Grätzel, M.; Hagfeldt, A. Dye-Sensitized Solar Cells for Efficient Power Generation under Ambient Lighting. *Nat. Photonics* **2017**, *11*, 372−378.

(9) Cao, Y.; Liu, Y.; Zakeeruddin, S. M.; Hagfeldt, A.; Grätzel, M. Direct Contact of Selective Charge Extraction Layers Enables High-Efficiency Molecular Photovoltaics. *Joule* **2018**, *2*, 1108−1117.

(10) Michaels, H.; Rinderle, M.; Freitag, R.; Benesperi, I.; Edvinsson, T.; Socher, R.; Gagliardi, A.; Freitag, M. Dye-sensitized solar cells under ambient light powering machine learning: Towards autonomous smart sensors for the internet of things. *Chem. Sci.* **2020**, *11*, 2895−2906.

(11) Fakharuddin, A.; Jose, R.; Brown, T. M.; Fabregat-Santiago, F.; Bisquert, J. A perspective on the production of dye-sensitized solar modules. *Energy Environ. Sci.* **2014**, *7*, 3952−3981.

(12) O'Regan, B.; Grätzel, M. A Low-Cost, High-Efficiency Solar Cell Based on Dye-Sensitized Colloidal TiO_2 Films. *Nature* **1991**, *353*, 737−740.

(13) Green, M.; Dunlop, E.; Hohl-Ebinger, J.; Yoshita, M.; Kopidakis, N.; Hao, X. Solar Cell Efficiency Tables (Version 57). *Prog. Photovolt.: Res. Appl.* **2020**, *29*, 3−15.

(14) Han, L.; Islam, A.; Chen, H.; Malapaka, C.; Chiranjeevi, B.; Zhang, S.; Yang, X.; Yanagida, M. High-Efficiency Dye-Sensitized Solar Cell with a Novel Co-Adsorbent. *Energy Environ. Sci.* **2012**, *5*, 6057−6060.

(15) Hardin, B. E.; Snaith, H. J.; McGehee, M. D. The Renaissance of Dye-Sensitized Solar Cells. *Nat. Photonics* **2012**, *6*, 162−169.

(16) Zeng, K.; Tong, Z.; Ma, L.; Zhu, W. H.; Wu, W.; Xie, Y. Molecular Engineering Strategies for Fabricating Efficient Porphyrin-Based Dye-Sensitized Solar Cells. *Energy Environ. Sci.* **2020**, *13*, 1617−1657.

(17) Mathew, S.; Yella, A.; Gao, P.; Humphry-Baker, R.; Curchod, B. F. E.; Ashari-Astani, N.; Tavernelli, I.; Rothlisberger, U.; Nazeeruddin, M. K.; Grätzel, M. Dye-Sensitized Solar Cells with 13% Efficiency Achieved through the Molecular Engineering of Porphyrin Sensitizers. *Nat. Chem.* **2014**, *6*, 242−247.

(18) Ji, J. M.; Zhou, H.; Eom, Y. K.; Kim, C. H.; Kim, H. K. 14.2% Efficiency Dye-Sensitized Solar Cells by Co-Sensitizing Novel Thieno-[3,2-b]Indole-Based Organic Dyes with a Promising Porphyrin Sensitizer. *Adv. Energy Mater.* **2020**, *10*, No. 2000124.

(19) Hattori, S.; Wada, Y.; Yanagida, S.; Fukuzumi, S. Blue Copper Model Complexes with Distorted Tetragonal Geometry Acting as Effective Electron-Transfer Mediators in Dye-Sensitized Solar Cells. *J. Am. Chem. Soc.* **2005**, *127*, 9648−9654.

(20) Kroon, J. M. *Energy Research Center Report*, ECN-C-05-078, 2005; pp 1−41.

(21) Liu, G.; Wang, H.; Li, X.; Rong, Y.; Ku, Z.; Xu, M.; Liu, L.; Hu, M.; Yang, Y.; Xiang, P.; Shu, T.; Han, H. A mesoscopic platinized graphite/carbon black counter electrode for a highly efficient monolithic dye-sensitized solar cell. *Electrochim. Acta* **2012**, *69*, 334−339.

(22) Kwon, J.; Park, N. G.; Lee, J. Y.; Ko, M. J.; Park, J. H. Highly efficient monolithic dye-sensitized solar cells. *ACS Appl. Mater. Interfaces* **2013**, *5*, 2070−2074.

(23) Behrouznejad, F.; Taghavinia, N.; Ghazyani, N. Monolithic dye sensitized solar cell with metal foil counter electrode. *Org. Electron.* **2018**, *57*, 194−200.

(24) Thompson, S. J.; Duffy, N. W.; Bach, U.; Cheng, Y. B. On the role of the spacer layer in monolithic dye-sensitized solar cells. *J. Phys. Chem. C* **2010**, *114*, 2365−2369.

(25) Kay, A.; Grätzel, M. Low cost photovoltaic modules based on dye sensitized nanocrystalline titanium dioxide and carbon powder. *Sol. Energy Mater. Sol. Cells* **1996**, *44*, 99−117.

(26) Vesce, L.; Riccitelli, R.; Mincuzzi, G.; Orabona, A.; Soscia, G.; Brown, T. M.; Di Carlo, A.; Reale, A. Fabrication of spacer and catalytic layers in monolithic dye-sensitized solar cells. *IEEE J. Photovolt.* **2013**, *3*, 1004−1011.

(27) Santos, F.; Hora, C.; Bernardo, G.; Ivanou, D.; Mendes, A. Efficient Monolithic Dye Sensitized Solar Cells with Eco-Friendly Silica-Titania Spacer Layers. *Sol. Energy* **2019**, *183*, 419−424.

(28) Maçaira, J.; Mesquita, I.; Andrade, L.; Mendes, A. Role of Temperature in the Recombination Reaction on Dye-Sensitized Solar Cells. *Phys. Chem. Chem. Phys.* **2015**, *17*, 22699−22710.

(29) Yella, A.; Lee, H.-W.; Tsao, H. N.; Yi, C.; Chandiran, A. K.; Nazeeruddin, M. K.; Diau, E. W.-G.; Yeh, C.-Y.; Zakeeruddin, S. M.; Grätzel, M. Porphyrin-Sensitized Solar Cells with Cobalt (II/III)−Based Redox Electrolyte Exceed 12 Percent Efficiency. *Science* **2011**, *334*, 629−634.
(30) Tsao, H. N.; Comte, P.; Yi, C.; Grätzel, M. Avoiding Diffusion Limitations in Cobalt(III/II)-Tris(2,2′- Bipyridine)-Based Dye-Sensitized Solar Cells by Tuning the Mesoporous TiO2 Film Properties. *ChemPhysChem* **2012**, *13*, 2976−2981.
(31) Kavan, L.; Yum, J. H.; Grätzel, M. Graphene nanoplatelets outperforming platinum as the electrocatalyst in co-bipyridine-mediated dye-sensitized solar cells. *Nano Lett.* **2011**, *11*, 5501−5506.
(32) Kim, C. K.; Kim, H. M.; Aftabuzzaman, M.; Jeon, I.-Y.; Kang, S. H.; Eom, Y. K.; Baek, J. B.; Kim, H. K. Comparative study of edge-functionalized graphene nanoplatelets as metal-free counter electrodes for highly efficient dye-sensitized solar cells. *Mater. Today Energy* **2018**, *9*, 67−73.
(33) Jeon, I.-Y.; Kim, H. M.; Kweon, D. H.; Jung, S.-M.; Seo, J.-M.; Shin, S.-H.; Choi, I. T.; Eom, Y. K.; Kang, S. H.; Kim, H. K.; Ju, M. J.; Baek, J.-B. Metalloid tellurium-doped graphene nanoplatelets as ultimately stable electrocatalysts for cobalt reduction reaction in dye-sensitized solar cells. *Nano Energy* **2016**, *30*, 867−876.
(34) Tsao, H. N.; Burschka, J.; Yi, C.; Kessler, F.; Nazeeruddin, M. K.; Grätzel, M. Influence of the interfacial charge-transfer resistance at the counter electrode in dye-sensitized solar cells employing cobalt redox shuttles. *Energy Environ. Sci.* **2011**, *4*, 4921−4924.
(35) Kim, J. C.; Rahman, M. M.; Ju, M. J.; Lee, J. J. Highly conductive and stable graphene/PEDOT:PSS composite as a metal free cathode for organic dye-sensitized solar cells. *RSC Adv.* **2018**, *8*, 19058−19066.
(36) Ahmad, S.; Bessho, T.; Kessler, F.; Baranoff, E.; Frey, J.; Yi, C.; Grätzel, M.; Nazeeruddin, M. K. A new generation of platinum and iodine free efficient dye-sensitized solar cells. *Phys. Chem. Chem. Phys.* **2012**, *14*, 10631−10639.
(37) Wang, H.; Feng, Q.; Gong, F.; Li, Y.; Zhou, G.; Wang, Z. S. In situ growth of oriented polyaniline nanowires array for efficient cathode of Co(III)/Co(II) mediated dye-sensitized solar cell. *J. Mater. Chem. A* **2013**, *1*, 97−104.
(38) Liu, I.; Hou, Y.; Li, C.; Lee, Y. Highly Electrocatalytic Counter Electrodes Based on Carbon Black for Cobalt(III)/(II)-Mediated Dye-Sensitized Solar Cells. *J. Mater. Chem. A* **2017**, *5*, 240−249.
(39) Stefik, M.; Yum, J. H.; Hu, Y.; Grätzel, M. Carbon-graphene nanocomposite cathodes for improved Co(ii/iii) mediated dye-sensitized solar cells. *J. Mater. Chem. A* **2013**, *1*, 4982−4987.
(40) Petrocco, A.; Liberatore, M.; Di Carlo, A.; Reale, A.; Brown, T. M.; Decker, F. Thermal Activation of Mass Transport and Charge Transfer at Pt in the I3−/I− Electrolyte of a Dye-Sensitized Solar Cell. *Phys. Chem. Chem. Phys.* **2010**, *12*, 10786−10792.
(41) Yue, G.; Wu, J.; Xiao, Y.; Huang, M.; Lin, J.; Lin, J. Y. High Performance Platinum-Free Counter Electrode of Molybdenum Sulfide-Carbon Used in Dye-Sensitized Solar Cells. *J. Mater. Chem. A* **2013**, *1*, 1495−1501.
(42) Burschka, J.; Brault, V.; Ahmad, S.; Breau, L.; Nazeeruddin, M. K.; Marsan, B.; Zakeeruddin, S. M.; Grätzel, M. Influence of the Counter Electrode on the Photovoltaic Performance of Dye-Sensitized Solar Cells Using a Disulfide/Thiolate Redox Electrolyte. *Energy Environ. Sci.* **2012**, *5*, 6089−6097.
(43) Lasia, A. Impedance of Porous Electrodes. *J. Electroanal. Chem.* **1995**, *397*, 27−33.
(44) Khelashvili, G.; Behrens, S.; Weidenthaler, C.; Vetter, C.; Hinsch, A.; Kern, R.; Skupien, K.; Dinjus, E.; Bo, H. Catalytic Platinum Layers for Dye Solar Cells: A Comparative Study. *Thin Solid Films* **2006**, *511−512*, 342−348.
(45) Arsyad, W. S.; Hidayat, R. Photovoltaic and Impedance Characteristics of Quasi Solid-State Dye-Sensitized Solar Cell Using Polymer Gel Electrolytes. *Adv. Mater. Res.* **2015**, *1112*, 256−261.
(46) Zhu, G.; Pan, L.; Yang, J.; Liu, X.; Sun, H.; Sun, Z. Electrospun nest-shaped TiO2 structures as a scattering layer for dye sensitized solar cells. *J. Mater. Chem.* **2012**, *22*, 24326−24329.
(47) Suresh, S.; Unni, G. E.; Ni, C.; Sreedharan, R. S.; Krishnan, R. R.; Satyanarayana, M.; Shanmugam, M.; Pillai, V. P. M. Phase Modification and Morphological Evolution in Nb2O5 Thin Films and Its Influence in Dye-Sensitized Solar Cells. *Appl. Surf. Sci.* **2017**, *419*, 720−732.
(48) Rams, J.; Tejeda, A.; Cabrera, J. M. Refractive Indices of Rutile as a Function of Temperature and Wavelength. *J. Appl. Phys.* **1997**, *82*, 994−997.
(49) Möls, K.; Aarik, L.; Mändar, H.; Kasikov, A.; Niilisk, A.; Rammula, R.; Aarik, J. Influence of Phase Composition on Optical Properties of TiO2: Dependence of Refractive Index and Band Gap on Formation of TiO2-II Phase in Thin Films. *Opt. Mater.* **2019**, *96*, No. 109335.
(50) Venkatesan, S.; Liu, I. P.; Hung, W. N.; Teng, H.; Lee, Y. L. Highly Efficient Quasi-Solid-State Dye-Sensitized Solar Cells Prepared by Printable Electrolytes for Room Light Applications. *Chem. Eng. J.* **2019**, *367*, 17−24.
(51) Venkatesan, S.; Liu, I. P.; Tseng Shan, C. M.; Teng, H.; Lee, Y. L. Highly Efficient Indoor Light Quasi-Solid-State Dye Sensitized Solar Cells Using Cobalt Polyethylene Oxide-Based Printable Electrolytes. *Chem. Eng. J.* **2020**, *394*, No. 124954.
(52) Higashino, T.; Imahori, H. Porphyrins as excellent dyes for dye-sensitized solar cells: recent developments and insights. *Dalton Trans.* **2015**, *44*, 448−463.
(53) Zeng, K.; Lu, Y.; Tang, W.; Zhao, S.; Liu, Q.; Zhu, W.; Tian, H.; Xie, Y. Efficient Solar Cells Sensitized by a Promising New Type of Porphyrin: Dye-Aggregation Suppressed by Double Strapping. *Chem. Sci.* **2019**, *10*, 2186−2192.
(54) Bella, F.; Galliano, S.; Gerbaldi, C.; Viscardi, G. Cobalt-Based Electrolytes for Dye-Sensitized Solar Cells: Recent Advances towards Stable Devices. *Energies* **2016**, *9*, No. 384.
(55) Koh, T. M.; Nonomura, K.; Mathews, N.; Hagfeldt, A.; Grätzel, M.; Mhaisalkar, S. G.; Grimsdale, A. C. Influence of 4-tert-Butylpyridine in DSCs with CoII/III Redox Mediator. *J. Phys. Chem. C* **2013**, *117*, 15515−15522.
(56) Phan, T. A. P.; Nguyen, N. P.; Nguyen, L. T.; Nguyen, P. H.; Le, T. K.; Van Huynh, T.; Lund, T.; Tsai, D. H.; Wei, T. C.; Nguyen, P. T. Direct Experimental Evidence for the Adsorption of 4-Tert-Butylpyridine and 2,2′-Bipyridine on TiO2 Surface and Their Influence on Dye-Sensitized Solar Cells'Performance. *Appl. Surf. Sci.* **2020**, *509*, No. 144878.
(57) Kim, J.; Kim, J. Y.; Lee, D.; Kim, B.; Kim, H.; Ko, M. J. Importance of 4-Tert -Butylpyridine in Electrolyte for Dye-Sensitized Solar Cells Employing SnO2 Electrode. *J. Phys. Chem. C* **2012**, *116*, 22759−22766.
(58) Lin, J.; Lien, C.; Chou, S. Multi-Wall Carbon Nanotube Counter Electrodes for Dye-Sensitized Solar Cells Prepared by Electrophoretic Deposition. *J. Solid State Electrochem.* **2012**, *16*, 1415−1421.
(59) Li, F.; Jennings, J. R.; Mathews, N.; Wang, Q. Evolution of Charge Collection/Separation Efficiencies in Dye-Sensitized Solar Cells Upon Aging: A Case Study. *J. Electrochem. Soc.* **2011**, *158*, B1158−B1163.
(60) Xiang, W.; Huang, W.; Bach, U.; Spiccia, L. Stable High Efficiency Dye-Sensitized Solar Cells Based on a Cobalt Polymer Gel Electrolyte. *Chem. Commun.* **2013**, *49*, 8997−8999.
(61) Ivanou, D. K.; Santos, R.; Maçaira, J.; Andrade, L.; Mendes, A. Laser assisted glass frit sealing for production large area DSCs panels. *Sol. Energy* **2016**, *135*, 674−681.
(62) Emami, S.; Martins, J.; Ivanou, D.; Mendes, A. Advanced Hermetic Encapsulation of Perovskite Solar Cells: The Route to Commercialization. *J. Mater. Chem. A* **2020**, *8*, 2654−2662.

https://doi.org/10.1021/acsaem.1c00616
ACS Appl. Energy Mater. 2021, 4, 5050−5058